A three dimensional Lagrangian analysis of the smoke plume from the 2019/2020 Australian wildfire event

Jezabel Curbelo[1] and Irina I. Rypina[2]

[1]Universitat Politècnica de Catalunya
[2]WHOI

November 24, 2022

Abstract

During the 2019/2020 bushfire season in Australia a rising plume, which had record concentration of smoke in the lower Stratosphere, was generated by the intense wildfires in southeast Australia. In this paper, we use the atmospheric wind reanalysis model ERA5 to characterize the three dimensional atmospheric transport in the region following a dynamical system approach in the Lagrangian framework. Aided by the Finite Time Lyapunov Exponent tool (FTLE) we identify Lagrangian Coherent Structures which simplify the three-dimensional transport description and make possible the characterization of the smoke plume evolution. Different reduced FTLE formulations are compared to study the impact of the vertical velocity and the vertical shear on the movement of the plume. Several examples of the LCS geometries are described and we show the presence of 3D lobe dynamics at play. Also, we unveil the qualitatively different dynamical fates of the smoke parcels trajectories depending on the region in which they originated.

Transport paths obtained with the inclusion of the buoyancy effects are compared with those obtained considering only the reanalysis velocity.

A three dimensional Lagrangian analysis of the smoke plume from the 2019/2020 Australian wildfire event

Jezabel Curbelo[1,2], **Irina I. Rypina**[3]

[1]Departament de Matemàtiques, Universitat Politècnica de Catalunya, Barcelona, Spain
[2]IMTech. Institute of Mathematics of UPC-BarcelonaTech, Barcelona, Spain
[3]Woods Hole Oceanographic Institution, 266 Woods Hole rd., Woods Hole, MA 02543, USA

Key Points:

- The impact of the vertical velocity and the vertical shear on the Lagrangian dynamics is described using different Finite Time Lyapunov Exponent (FTLE) formulations.
- A three dimensional lobe dynamics is detected in the atmosphere during the Australian wildfire 2019/2020 event.
- Lagrangian Coherent regions where trajectories have qualitatively different dynamical fates are characterized with and without considering buoyancy effects

Corresponding author: Jezabel Curbelo, `jezabel.curbelo@upc.edu`

Abstract

During the 2019/2020 bushfire season in Australia a rising plume, which had record concentration of smoke in the lower Stratosphere, was generated by the intense wildfires in southeast Australia. In this paper, we use the atmospheric wind reanalysis model ERA5 to characterize the three dimensional atmospheric transport in the region following a dynamical system approach in the Lagrangian framework. Aided by the Finite Time Lyapunov Exponent tool (FTLE) we identify Lagrangian Coherent Structures which simplify the three-dimensional transport description and make possible the characterization of the smoke plume evolution. Different reduced FTLE formulations are compared to study the impact of the vertical velocity and the vertical shear on the movement of the plume. Several examples of the LCS geometries are described and we show the presence of 3D lobe dynamics at play. Also, we unveil the qualitatively different dynamical fates of the smoke parcels trajectories depending on the region in which they originated. Transport paths obtained with the inclusion of the buoyancy effects are compared with those obtained considering only the reanalysis velocity.

1 Introduction

The measuring and understanding of air pollutant transport is a challenge due to many factors, including the complexity of atmospheric winds, finite size of the pollutant particles, or chemical composition of the pollutant (Harriss et al., 1984; Evangeliou et al., 2020; von Schoenberg et al., 2021). A variety of processes acting on different scales are needed to be modeled with high resolution and accuracy throughout an extensive geographic domain in order to predict a movement of a pollutant plume in the atmosphere. The analysis of individual trajectories is sensitive to small errors in velocity forecasts, for that reason it is a common practice to instead rely on statistical techniques or dynamical systems analysis to understand the underpinnings of transport. Lagrangian Coherent Structures (LCS) - a concept introduced by Haller and Yuan (2000)- are material curves or surfaces that delineate the evolution of any advective tracer over a time interval of interest. Hence, they act as transport barriers and shape both local and global transport. There are several tools to approximate LCS such as Finite-Size Lyapunov Exponent (FSLE)(Artale et al., 1997; Aurell et al., 1997), Lagrangian descriptors (Mancho et al., 2013; Lopesino et al., 2017; García-Garrido et al., 2018), trajectory complexity (Rypina et al., 2011), spectral clustering (Hadjighasem et al., 2016), Objective Eulerian CS (Serra & Haller, 2016) and other methods (Rypina & Pratt, 2017; Schlueter-Kuck & Dabiri, 2017; Mezić et al., 2010; Haller & Beron-Vera, 2012; Farazmand & Haller, 2012; Haller et al., 2016, 2018). We will use the Finite Time Lyapunov exponent (FTLE)(Haller & Yuan, 2000; Haller, 2002) because it is widely used, frame-independent, and easy to compute and interpret. Although FTLEs have been shown to produce false negatives for LCS in shear-dominated flows (Haller, 2015), this classical dynamical systems tool seems to work well in our application.

The stratospheric circulation, chemical air composition, or radiative balance may be affected by the episodic events such as wildfires that generate an intense smoke patch (Solomon et al., 2022; Duncan et al., 2003; Khaykin et al., 2018; Yu et al., 2021; Stocker et al., 2021; Peterson et al., 2021). Thus, understanding the movement and evolution of a smoke plume is important for predicting and anticipating the local and global effects that it would produce.

The 2019/2020 bushfire season in Australia was marked by several unprecedented events such as extreme positive phase of the Indian Ocean Dipole (IOD) (Ratna et al., 2021; Wang & Cai, 2020; Cai et al., 2009), associated with the suppression of precipitation over western Australia (Saji et al., 1999; Yang et al., 2015; Deb et al., 2020), or an unusually weak stratospheric polar vortex in the Southern Hemisphere during that period (Lim et al., 2019, 2021) which could have lead to hot and dry weather over Australia. The Australian New Year (ANY) 2019 event caused a burn area of approximately 21% of Australia's temperate forests (Boer et al., 2020). The fires were extremely large in scale and intensity (van der

Velde et al., 2021) and created a record concentration of smoke in the Lower Stratosphere (D'Angelo et al., 2022; Khaykin et al., 2020; Kablick et al., 2020) that was larger than the previous record in mid-August 2017 (Peterson et al., 2018) during the Pacific Northwest PyroCb Event (PNE). The largest smoke plumes exhibited a rapid ascent from the lower (around 15-16 km) to the upper stratosphere (altitudes above 31km) in less than two months (Khaykin et al., 2020) and have persisted for more than 15 months encircling a portion of the Southern Hemisphere and altering the dynamic circulation (Allen et al., 2020; Khaykin et al., 2020; Kablick et al., 2020; Peterson et al., 2021).

We focus our study on three periods of time representative of the three phases of the smoke plume event: the start of the first pyroCb event start (later December); the time when the cloud reaches a highest concentration of smoke (early January), and near the end of the event almost two months later to see how the particles have persisted in the stratosphere (end of February). Following a Lagrangian approach, we are going to search for LCS in the southern Hemisphere atmosphere during the ANY2019 event.

This paper is organized as follows. Section 2 describes the dataset used in our study. Section 3 shows a comparison of the FTLE in 2D and 3D. Results on the wildfire smoke plume movement in the atmosphere during the 2019/2020 Australian bushfire season are presented in section 4. Finally, Section 5 presents our conclusions.

2 Data

Our Lagrangian analysis is based on the ERA5 reanalysis dataset, the fifth generation of the European Centre for Medium-Range Weather Forecasts (ECMWF) atmospheric reanalysis produced by the global climate Copernicus Climate Change Service (C3C) (Hersbach et al., 2019). The ERA5 provides lateral wind velocity $\vec{v}$ (m/s), vertical velocity ω (Pa/s), geopotential, and temperature in 37 pressure levels from 1000hPa to 1hPa. The temporal resolution is one hour.

The ECMWF provides the vertical velocity ω in Pa/s with negative values corresponding to upward motion. To compute the vertical velocity in meters per second we use the hydrostatic approximation which assumes that the horizontal scale is larger compared to the vertical one, i.e.

$$\omega = -\rho g w \tag{1}$$

where ρ is the density, g is the gravity, and w is the vertical velocity in m/s. Here, the density is related to pressure P and the temperature T through the equation of state of the ideal gases, $P = R\rho T$ with $R = 287.058$ (m^2/s^2K^{-1}).

In order to track the movement of the real observed plumes of smoke in the stratosphere we use the EOS Aura Microwave Limb Sounder (MLS) Level 2 standard product for geopotential height. The data version used is 5.0 (Schwartz et al., 2020). MLS provides day and night near-global (82°S- 82°N) measurement of vertical profiles of various atmospheric gaseous compounds geopotential height, and temperature of the atmosphere. The measurements yield around 3500 profiles per day for each species with a vertical resolution of approximate 3-6 km. Following Kablick et al. (2020), we use the information of the water vapor mixing ratio H_2O, the collocated carbon monoxide mixing ratio CO and the geopotential height from the Microwave Limb Sounder (MLS) dataset. The plume is represented by the values that correspond to MLS profil $\mathrm{H_2O} > 7$ ppmv, CO > 50 ppbv and geopotential height between 15km and 35km.

To study the spatial and temporal distribution of thermal anomalies during the Australian bushfire season 2019/2020 and to detect active fire locations we also use the Ozone Mapping and Profiler Suite (OMPS) Aerosol Index (AI) from NASA's Fire Information for Resource Management System (FIRMS, 2022) and the Visible Infrared Imaging Radiometer Suite Fire data (VIIRS, 2022).

3 Lagrangian Methods

We work in the Lagrangian framework, that is, we analyze stratospheric transport following pollutant parcels trajectories. We look for LCS which control the stretching and folding of the polluted air mass and separate regions where trajectories have qualitatively different dynamical fates. The method that we use to approximate LCS is the Finite Time Lyapunov exponent (FTLE) (Shadden et al., 2005; Haller & Yuan, 2000; Haller, 2002) which measures the exponential separation rate between initially nearby air parcels.

Let $\mathbf{x}(t;\mathbf{x}_0)$ be a trajectory of an air parcel that starts at $\mathbf{x}_0$ at time t_0 :

$$\frac{d\mathbf{x}}{dt} = \mathbf{v}(\mathbf{x}, t) \tag{2}$$

where $\mathbf{v}(\mathbf{x}, t)$ is the velocity vector field. Thus,

$$\mathbf{x} = \mathbf{x}_0 + \int_{t_0}^{\tau} \mathbf{v} dt.$$

Let F be the strain tensor given by

$$F = \frac{\partial \mathbf{x}}{\partial \mathbf{x}_0} = I + \int_{t_0}^{\tau} \frac{\partial \mathbf{v}}{\partial \mathbf{x}} \cdot \frac{\partial \mathbf{x}}{\partial \mathbf{x}_0} dt,$$

and $G = F^{\intercal} F$ be the right Cauchy-Green tensor. The FTLE is defined by

$$\Lambda(x_0, t_0; \tau) = \frac{\log \sqrt{\lambda_{max}(G)}}{\tau - t_0} \tag{3}$$

where $\lambda_{max}(G)$ is the maximum eigenvalue of the matrix G. Repelling LCS are defined as maximizing ridges of the FTLE field computed from forward trajectories (final time $t_f > t_0$), and attracting LCS are defined as ridges in the backward-time ($t_f < t_0$) FTLE field. The repelling and attracting LCS identified in this manner are proxies for the finite-time counterparts of the stable and unstable manifolds of hyperbolic trajectories from the classical theory of dynamical systems. Thus, FTLE field are usually considered as indicators of hyperbolic LCSs (Haller, 2001) despite they can produce both false positives, where separation is due to shear and not hyperbolic behavior, and negatives in LCS detection (Haller, 2002, 2011) even in simple two-dimensional steady flows (Haller, 2011; Farazmand & Haller, 2012). Despite this limitation, in our case FTLEs seem to be a useful tool that produces physically-relevant partitions of the domain.

3.1 Validity of different formulations of FTLEs in the atmospheric flows

In geophysical flows the full computation of the evolving 3D velocity field is challenging, and the vertical velocity, which is generally much smaller than the horizontal velocities, is often estimated as a diagnostic quantity (rather than prognostically solved as part of the equations of motion like the horizontal velocity components) and is thus less reliable. It is thus tempting to ignore $w-$velocity in the computation of FTLEs. However, as we show below, such approach leads to large errors in situations where vertical shear of horizontal velocity is large.

In order to investigate the effects of the vertical velocity and vertical shear on the resulting FTLEs and LCS, following Sulman et al. (2013), we compare the reduced FTLE formulations given by the definitions:

Case 1. 2D form of tensor G with trajectories from 2D, $\mathbf{x} = (x, y) \in \mathbb{R}^2$, i.e.

$$FTLE_{2D} = \frac{\log \sqrt{\lambda_{max}(G_1)}}{\tau - t_0} \text{ with } G_1 = F_1^{\intercal} F_1 \text{ and } F_1 = \begin{bmatrix} \frac{\partial x}{\partial x_0} & \frac{\partial x}{\partial y_0} & 0 \\ \frac{\partial y}{\partial x_0} & \frac{\partial y}{\partial y_0} & 0 \\ 0 & 0 & 1 \end{bmatrix} \tag{4}$$

Case 2. Case 1 using 3D trajectories $\mathbf{x} = (x, y, z) \in \mathbb{R}^3$, i.e.

$$FTLE_{2D_{3D}} = \frac{\log \sqrt{\lambda_{max}(G_2)}}{\tau - t_0} \text{ with } G_2 = F_2^{\intercal} F_2 \text{ and } F_2 = \begin{bmatrix} \frac{\partial x}{\partial x_0} & \frac{\partial x}{\partial y_0} & 0 \\ \frac{\partial y}{\partial x_0} & \frac{\partial y}{\partial y_0} & 0 \\ 0 & 0 & 1 \end{bmatrix} \quad (5)$$

Case 3. 2D form of tensor G with vertical velocity and trajectories from 3D, $\mathbf{x} = (x, y, z) \in \mathbb{R}^3$, i.e.

$$FTLE_{vel} = \frac{\log \sqrt{\lambda_{max}(G_3)}}{\tau - t_0} \text{ with } G_3 = F_3^{\intercal} F_3 \text{ and } F_3 = \begin{bmatrix} \frac{\partial x}{\partial x_0} & \frac{\partial x}{\partial y_0} & 0 \\ \frac{\partial y}{\partial x_0} & \frac{\partial y}{\partial y_0} & 0 \\ \frac{\partial z}{\partial x_0} & \frac{\partial z}{\partial y_0} & 1 \end{bmatrix} \quad (6)$$

Case 4. 2D form of tensor G with vertical shear and trajectories from 2D, i.e.

$$FTLE_{shear_{2D}} = \frac{\log \sqrt{\lambda_{max}(G_4)}}{\tau - t_0} \text{ with } G_4 = F_4^{\intercal} F_4 \text{ and } F_4 = \begin{bmatrix} \frac{\partial x}{\partial x_0} & \frac{\partial x}{\partial y_0} & \frac{\partial x}{\partial z_0} \\ \frac{\partial y}{\partial x_0} & \frac{\partial y}{\partial y_0} & \frac{\partial y}{\partial z_0} \\ 0 & 0 & 1 \end{bmatrix} \quad (7)$$

Case 5. Case 4 using 3D trajectories $\mathbf{x} = (x, y, z) \in \mathbb{R}^3$, i.e.

$$FTLE_{shear_{3D}} = \frac{\log \sqrt{\lambda_{max}(G_5)}}{\tau - t_0} \text{ with } G_5 = F_5^{\intercal} F_5 \text{ and } F_5 = \begin{bmatrix} \frac{\partial x}{\partial x_0} & \frac{\partial x}{\partial y_0} & \frac{\partial x}{\partial z_0} \\ \frac{\partial y}{\partial x_0} & \frac{\partial y}{\partial y_0} & \frac{\partial y}{\partial z_0} \\ 0 & 0 & 1 \end{bmatrix} \quad (8)$$

Case 6. 3D form of tensor G with trajectories $\mathbf{x} = (x, y, z) \in \mathbb{R}^3$, i.e.

$$FTLE_{3D} = \frac{\log \sqrt{\lambda_{max}(G_6)}}{\tau - t_0} \text{ with } G_6 = F_6^{\intercal} F_6 \text{ and } F_6 = \begin{bmatrix} \frac{\partial x}{\partial x_0} & \frac{\partial x}{\partial y_0} & \frac{\partial x}{\partial z_0} \\ \frac{\partial y}{\partial x_0} & \frac{\partial y}{\partial y_0} & \frac{\partial y}{\partial z_0} \\ \frac{\partial z}{\partial x_0} & \frac{\partial z}{\partial y_0} & \frac{\partial z}{\partial z_0} \end{bmatrix} \quad (9)$$

We compare the different formulations of FTLE using air parcel trajectories restricted to 2D (case 1 and 3) or allowing the air particles to move in three-dimensional space (case 2) and also with and without the terms in F associated with the vertical shear (3rd column) and/or vertical velocity (3rd row).

For the computation of the FTLE, trajectories are determined by integrating the differential equation (2) using the Cash-Karp method with fixed step size of one hour, which provides estimates accurate to fifth order. The derivatives in the Cauchy-Green tensors are then approximated using second-order centered finite-differences and the eigenvalues are calculated with the MATLAB function *eig* that use the QZ algorithm also known as the generalized Schur decomposition. For the FTLE study in this section, trajectories are estimated over a time interval of 5 days, which is sufficiently long for the ridges in FTLE fields to become well-defined, but sufficiently short to not produce overly complex and tangled ridges.

The stable manifolds (repelling structures) are calculated through FTLE using forward trajectories. The unstable manifolds (attracting structures) are calculated through FTLE using backward trajectories. In the figures below, we represent repelling structures in blue and attracting structures in red.

Since we are working in the atmosphere, we change our coordinate system from Cartesian to spherical. Therefore the matrix F has the following form,

$$F = \begin{bmatrix} \dfrac{r\sin(\theta)}{r_0\sin\theta_0}\dfrac{\partial\varphi}{\partial\varphi_0} & \dfrac{r\sin\theta}{r_0}\dfrac{\partial\varphi}{\partial\theta_0} & r\sin(\theta)\dfrac{\partial\varphi}{\partial r_0} \\ \dfrac{r}{r_0\sin\theta_0}\dfrac{\partial\theta}{\partial\varphi_0} & \dfrac{r}{r_0}\dfrac{\partial\theta}{\partial\theta_0} & r\dfrac{\partial\theta}{\partial r_0} \\ \dfrac{1}{r_0\sin\theta_0}\dfrac{\partial r}{\partial\varphi_0} & \dfrac{1}{r_0}\dfrac{\partial r}{\partial r_0} & \dfrac{\partial r}{\partial r_0} \end{bmatrix}$$

where r is from the Earth center height, θ is a function of the latitude and ϕ is longitude.

Figure 1 shows the different cases of forward FTLE (first column) and backward FTLE (second column) computed with $\tau = 5$ days at 5km height. Case 1 and Case 2 are too low in magnitude compared to Case 6. These cases ignore the vertical velocity and the vertical shear overestimating large-scales LCS and under-estimate small scales. This seems to be less important in the Polar jet region south of about 40°S, which is dominated by the large-scale LCS, but it seems to lead to large discrepancies north of 40°S, including region over Australia, where small scales nearly erase the large-scale ridges seen in the upper 2 rows of Fig. 1. Case 3, which considers vertical velocity but ignoring vertical gradients, is also too low in magnitude showing the same issues as case 2. On the contrary, Case 4 which includes the effects of vertical shear in the horizontal velocity components, improves in magnitude and captures the larger-scale LCS structure but still misses small scales, especially in the north of the domain. Case 5 is pretty close to Case 6 (i.e., full 3D formulation of FTLEs).

The drastic improvement of Case 5 compared to Case 3 suggests that the influence of vertical shear on the spread of 3D trajectories is much more important than the influence of vertical velocity. The significant improvement of Case 5 over Case 4 highlights the significant differences between the lateral spread of 3D trajectories versus 2D trajectories and thus points to the importance of using 3D trajectories in the computation of FTLEs. It is thus extremely important to both use 3D trajectories and include the terms corresponding to the vertical shear in the computation of FTLEs. This is similar to the situation in the ocean at submesoscale, but in ocean mesoscale flows, Case 4 is typically closer to Case 5 (Lanotte et al., 2016; McWilliams, 2016; Sulman et al., 2013). Therefore, in what follows, we use the full 3D formulation given by (9).

4 Results

We focus our analysis on three time periods, the aerosol injection (late December), the evolution of the smoke plume that dispersed into several separate patch and reached high levels in the stratosphere (early January - mid February), and when the persistent path of that plume topped above 31km (late February).

4.1 Late December 2019: Direct injection into the extratropical stratosphere

Several wildfires contributed to the first relatively small pyroCb event around 22 December 2019 (Peterson et al., 2021). Using the Ozone Mapping and Profiler Suite (OMPS) Aerosol Index from NASA's Fire Information for Resource Management System (Flynn et al., 2014), panel (a) of Figure 2 shows the Absorbing Aerosol Index (AAI) highlighting the smoke plume generated by this first aerosol injection. Similarly, panel (b) shows the plume generated by the main injection on 31 December 2019. The red dots in the figure indicate active fire detections and thermal anomalies; maroon color is the plume. In this section we mapped out LCS over and around Australia on December 22. Our goal here was two-fold: first, we wanted to see what sort of the 3D LCS geometries existed in the stratosphere at the time of first smoke injection; and second, whether any of these structures were influencing the movement of the actual smoke plume. The first question is more of a generic study of possible 3D LCS geometries in the stratosphere, while the second question is more applied.

Figure 3(a-b) shows two slices of the 3D forward FTLE computation: a horizontal slice longitude-latitude at 11km height (panel a) and a vertical latitude-height section at 140°E (b). Several geometric structures are highlighted by the maximizing ridges of FTLE. The blue box shows barriers over Australia that divide horizontally the region into three parts, north, central and south. The red box highlights the barrier cutting off the very southernmost tip of Australia. And the black box contains the structures living at the northern edge of the stratospheric polar jet. We describe the geometry of these structures in 3D and the behavior of the fluid parcels in their neighborhoods.

The simplest geometric structure lives inside the red box. This feature resembles a vertically-tilted curtain spanning about 8 km in vertical, from ~ 5 to 13 km. South of this barrier, move rapidly to the east, generally maintaining or even increasing their altitude (with a bit of altitude decrease at the end of 5 days). North of this barrier, the parcels also move to the east, but with more northward deviation, much more slowly, and at a generally lower altitude (see an example of the trajectories in Fig. 3(e)).

The LCS inside the blue box in figure 3 has a slightly more complex vertical structure. This structure, shaped like a hat, acts as a lid preventing upwards vertical transport. This cap-like structure divides Australia into three regions as shown in panel (c) and (d). Parcels that originate outside the hat (i.e., to the north and south of the blue ridge in the blue box of in Fig. 3a-b) move eastward increasing or maintaining height. However, parcels that originate inside the structure move west and down.

Finally, the LCS inside the black box has the most interesting geometry out of the three. Topologically, it is a tube that is closed at its western end. This tube structure seems to also interact with the nearby eddy located to the northeast of it, and with another eddy located further to the southeast. An example of two trajectories inside and outside the tube is shown in Fig. 3(f) but the dynamic in the neighborhood of this tube-shaped structure is more complex and requires a more in-depth study.

First and second column of Figure 4 show four daily snapshots of the forward (blue) and backward (red) FTLEs at 11 km height near the tubular structure from 22 to 25 of December. The third column of Fig. 4 is a schematic diagram showing the intersecting attracting and repelling LCS near the tube. The Lagrangian geometry in this region is governed by two hyperbolic trajectories (HT1 and HT2) that give rise to two pairs of intersecting stable and unstable manifolds. (The stable and unstable manifolds of HT1/HT2 are shown in purple/blue and red/orange). The tube is nothing other than a lobe that is trapped by a segment of unstable manifold of HT1 and a stable manifold of HT2. Initially, this lobe is close to HT1 but moves towards HT2 with time. As it does so, the segment of its bounding unstable manifold elongates, and the segment of the stable manifold shrinks, so as the tube moves away from HT1, it gets shorter and wider. Later on, as it approaches HT2, it becomes stretched along the unstable manifold of HT2 and becomes narrow and long again. This is a classical picture of a heteroclinic tangle, which suggests that the 3D turnstyle lobe mechanism is a common phenomenon in the stratosphere.

The behavior of the different sets of particles in and around the tube is also shown in figure 4. The yellow dots correspond to particles that are released inside the nearby northeastern eddy. The black and green particles are released inside and outside the tube, respectively. These particles move eastward following first the stable and unstable manifold of HT1 and later, the stable manifold of HP2. On 24 Dec 2019 they approach HT2, and their route is interrupted by the unstable manifold of the HT2. From there on, black and green parcels diverge and move in different directions, as seen in Fig. 4.

Our rendition of the 3D geometry of the manifolds bounding the tube is shown in Fig. 5a, where we stacked LCS in different horizontal slices vertically to produce a 3D picture. To extract the maximizing ridges of the FTLE field we have used a 2D edge detection algorithm on each horizontal slice (every 500m in the vertical direction) in combination with vertical slices (every 5 degrees of longitude and latitude). The edge detection algorithm in 2D used is the method of Canny (1986). We then advected the surfaces in time to see if their behavior matches our description above. The temporal evolution of these advected surfaces shows that the elongated blue tubular structure becomes shorter (see panel b) as it approaches HT2 on Dec 25 (confirming what we already saw in Figs. 4).

The presence of the three structures studied in this section were important for the actual smoke plume on Dec 22 which mainly falls on top of the area with many tangled FTLEs ridges east of Australia, as shown in panel (g) of Figure 3. Such regions mark areas of rapid stirring and mixing which suggests that the plume overlaying that region on Dec 22nd will disperse and will be unlikely to stay coherent for long. Another small part of the aerosol plume was located over north of the curtain-like manifold in the red box and so was expected to behave like the northern trajectory in Fig. 3(e).

4.2 Early January 2020: Stratospheric Evolution

The observed plume was visible from satellites, although with limited resolution. Over 1-4 January parts of the plume were detected moving to the southeast from Australia, and on January 6th a very coherent patch was identified near 120W; 50N (Kablick et al., 2020).

Figure 6(a) shows the observed plume, as detected from the satellite, on Jan 7th and onward. On Jan 6th, the highly concentrated plume reaching roughly 1000 km in diameter was detected in the stratosphere at about 15 km near 100W,60S. From there, the smoke plume split into two parts that moved along two different paths (Kablick et al., 2020). Path P2 (blue dashed line in Fig. 6a) was eastward at a nearly constant height of about 17 km, whereas path P1 (green solid curve in Fig. 6a) looped around and went westward, ascending on its way and passing south.

Motivated by the splitting of the plume on Jan 6th and the striking difference between the P1 and P2 paths, we have applied the Lagrangian approach to better understand the cause of the splitting, the subsequent transport geometry, and the influence of the plume buoyancy on its movement.

Consistent with observations, simulated parcels in the ERA5 model released in the area of the observed plume (black box in Fig. 6) on Jan 6th also showed the splitting into two distinct P1-like and P2-like groups. Without the buoyancy effects, however, the P1 path is too low in altitude, is shifted northward, and passes over Australia rather than south of Australia on Feb 26, as in observations. Using the difference in altitude between the simulated and observed P1 trajectories on Feb 26th, we have estimated the time-averaged buoyant velocity to be about 0.0022 m/s. When this buoyant velocity was added to the ERA5 velocities, the agreement with observations significantly improved. With buoyancy, P1-like path shifted up and south, with P1-like trajectories passing south of Australia by Feb 26th, consistent with observations. Advecting P1-like trajectories backward in time (with negative buoyancy of 0.0052 m/s) from Jan 6, we observed that these passed just to the southeast Australia on Dec 31st, i.e., right within the area of the observed plume of the main ANY event (see Fig. 2b right). This suggests that the plume observed on Jan 6th was likely generated by the main event on Dec 31, rather than the earlier event of Dec. 22. This also agrees with our previous conclusion that the plume generated on Dec 22nd was unlikely to stay coherent for long.

The splitting of the plume into P1 and P2 on Jan 6 suggested the presence of strong LCS in the area at that time, which acted as transport barriers with different trajectory fates for parcels on the opposite sides of LCS. Indeed, the FTLE map (both with and without buoyancy) showed a number of maximizing ridges, i.e., proxy LCS, delineating the region into areas with qualitatively different behavior of fluid parcels. The LCS and the schematics of trajectories are shown in Fig. 7. Of main interest to us are the red and purple/magenta trajectories which are representative of the P1 and P2 paths, respectively. The former originate from the eddy-like feature centered at around 125W,55N with two long and narrow tendrils extending from it. The latter originate in the eastern part of the domain and are separated from the rest by a strong FTLE ridge, which has a tilted-curtain-line geometry in 3D spanning the altitudes of the observed plume (16-22 km).

It is interesting to look at the changes in LCS geometry with the addition of buoyancy. Without buoyancy, the eddy only contains a small percentage of P1-like trajectories (red), with most parcels (yellow) continuing westward, rather than eastward after looping around. With buoyancy, however, almost the entire eddy becomes red. This is because buoyant parcels rise up higher and are then carried westward by the strong westward winds at higher altitudes.

4.3 Late February 2020: Smoke path in the upper stratosphere

By 26 February the smoke plume reached above 31 km (see panel (a) in figure 6, path P1) and formed a long and narrow nearly zonal filament located south-southwest of Australia. In this section, we turn our attention to mapping out the attracting LCS on Feb 26 that were responsible for this observed stretching. Indeed, the backward FTLEs (proxi attracting LCS) on Feb 26 are dominated by yet another tilted-curtain-like FTLE ridge spanning the altitudes of the plume (30-33 km), with the locations of the forward-tracked (from Jan 6 to Feb 26) air parcels (red dots) showing a clear alignment with the ridge (Both FTLEs and trajectories were computed including buoyancy effects.) The ridge seems to weaken slightly with altitude, so the alignment of trajectories is also weaker higher up in the stratosphere. These features can be seen in the figure 8.

5 Conclusions

Motivated by the strong Australian wildfire event in 2019/2020, we have applied the Lagrangian approach to study the 3D transport in the stratosphere. The study is based on the ERA5 reanalysis winds and compares simulations of the smoke plume with available observations.

The stratospheric winds have relatively weak vertical velocities compared to horizontal velocities. It is thus tempting to ignore w and consider the motion of air parcels in 2D. However, as we have shown using different formulations of FTLEs in this paper, such quasi-2D approach is misleading as it does not take into account the fact that even slight vertical movement might expose air parcels to different horizontal advection due to strong vertical shear. Thus, for an accurate representation of 3D transport, it is necessary to consider the movement of trajectories in 3D, and, importantly, include the vertical shear terms in the formulation of the FTLE matrix. On the other hand, due to the smallness of vertical displacement of trajectories, the terms associated with the vertical movement itself can be safely ignored, so the formulation of FTLEs can be reduced from 3x3 matrix to the 2x3 matrix without much reduction in accuracy.

We then used the FTLEs (computed using 3D trajectories and with the inclusion of vertical shear) to map out the dominant LCS on different days in Dec 2019-Feb 2020 to understand the movement and behavior of the observed plume.

First, we looked at LCS on Dec 22, the date of one of the major bushfire events that year. On that day, we found several types of LCS geometries present in the stratosphere near Australia. The most interesting of them from the dynamical systems perspective was a tube-like LCS, which turned out to be a lobe formed by the intersecting manifold of two hyperbolic trajectories. Although fully three-dimensional, the lobe moved in a manner that was consistent with a heteroclinic tangle geometry, suggesting that lobe dynamics and turnstyle lobe mechanism might be important in the stratosphere. Superimposing the plume on top of the mapped FTLEs on Dec 22 showed that it was mainly located in a region characterized by many tangled LCS, suggesting that this particular plume would not be expected to stay coherent for long and would disperse quickly.

We then mapped out LCS on Jan 6th, the day when a very coherent smoke patch was detected from satellites almost half-way across the globe from Australia. This patch was then observed to split into two parts, one moving eastward at low altitude and another looping around and heading westward back towards Australia at much higher altitudes. Analysis of simulated trajectories in the ERA5 reanalysis model suggested that the movement of the plume was strongly affected by positive buoyancy of hot smoke. With buoyancy included, simulated plume matched the observed one very well (without buoyancy, it did not). We then used the simulated trajectories with buoyancy to map out LCS on Jan 6th, which clearly delineated regions destined to take two different paths. We also backtracked trajectories (with negative buoyancy) from Jan 6 backward in time to see which of the two first smoke injection events (Dec 22 or Dec 31) produced this observed coherent patch on Jan 6. The result clearly pointed to the Dec 31 event as the origin of this patch.

Finally, we mapped out LCS on Feb 26, and observed that the smoke plume at that time was aligning with a nearly zonal attracting FTLE ridge. Overall, this suggests that FTLEs might be a useful tool in understanding and predicting the evolution of a pollutant patch, specific for the 2019/2020 bushfire event studied here, or more generally in other atmospheric applications.

Acknowledgments

We acknowledge the use of data and imagery from NASA's Fire Information for Resource Management System (FIRMS) (`https://earthdata.nasa.gov/firms`), part of NASA's Earth Observing System Data and Information System (EOSDIS). CALIOP, OMPS, and MLS data are available from NASA's Earthdata system at `https://urs.earthdata.nasa.gov/`. JC acknowledges the support of the RyC project RYC2018-025169, the Spanish grant PID2020-114043GB-I00 and the 2020/2021 "L'Oréal-UNESCO For Women in Science" Fellowship (L'Oréal Spain), IR would like to acknowledge support from ONR Grant N000141812417 and NSF grant OCE-2124210. We also thank Prof. Caroline Ummenhofer for useful initial comments.

References

Allen, D. R., Fromm, M. D., III, G. P. K., & Nedoluha, G. E. (2020). Smoke with induced rotation and lofting (swirl) in the stratosphere. *Journal of the Atmospheric Sciences*, *77*(12), 4297 - 4316. doi: 10.1175/JAS-D-20-0131.1

Artale, V., Boffetta, G., Celani, A., Cencini, M., & Vulpiani, A. (1997). Dispersion of passive tracers in closed basins: Beyond the diffusion coefficient. *Physics of Fluids*, *9*(11), 3162-3171.

Aurell, E., Boffetta, G., Crisanti, A., Paladin, G., & Vulpiani, A. (1997). Predictability in the large: an extension of the concept of Lyapunov exponent. *Journal of Physics A: Mathematical and General*, *30*(1), 1–26.

Boer, M. M., de Dios, V. R., & Bradstock, R. A. (2020). Unprecedented burn area of australian mega forest fires. *Nature Climate Change*, *10*(3), 171–172.

Cai, W., Cowan, T., & Raupach, M. (2009). Positive Indian Ocean dipole events precondition southeast Australia bushfires. *Geophysical Research Letters*, *36*(19).

Canny, J. (1986). A computational approach to edge detection. *IEEE Transactions on pattern analysis and machine intelligence*(6), 679–698.

Deb, P., Moradkhani, H., Abbaszadeh, P., Kiem, A. S., Engström, J., Keellings, D., & Sharma, A. (2020). Causes of the widespread 2019–2020 Australian bushfire season. *Earth's Future*, *8*(11), e2020EF001671.

Duncan, B. N., Bey, I., Chin, M., Mickley, L. J., Fairlie, T. D., Martin, R. V., & Matsueda, H. (2003). Indonesian wildfires of 1997: Impact on tropospheric chemistry. *Journal of Geophysical Research: Atmospheres*, *108*(D15).

D'Angelo, G., Guimond, S., Reisner, J., Peterson, D. A., & Dubey, M. (2022). Contrasting stratospheric smoke mass and lifetime from 2017 canadian and 2019/2020 australian megafires: Global simulations and satellite observations. *Journal of Geophysical Research: Atmospheres*, *127*(10), e2021JD036249. doi: https://doi.org/10.1029/2021JD036249

Evangeliou, N., Grythe, H., Klimont, Z., Heyes, C., Eckhardt, S., Lopez-Aparicio, S., & Stohl, A. (2020). Atmospheric transport is a major pathway of microplastics to remote regions. *Nature communications*, *11*(1), 1–11.

Farazmand, M., & Haller, G. (2012). Computing lagrangian coherent structures from their variational theory. *Chaos: An Interdisciplinary Journal of Nonlinear Science*, *22*(1), 013128. doi: 10.1063/1.3690153

FIRMS. (2022). *NASA fire information for resource management system.* `https://rms.modaps.eosdis.nasa.gov/map/`. ([Online; accessed 25-May-2022])

Flynn, L., Long, C., Wu, X., Evans, R., Beck, C. T., Petropavlovskikh, I., ... Seftor, C. (2014). Performance of the ozone mapping and profiler suite (omps) products. *Journal of Geophysical Research: Atmospheres*, *119*(10), 6181-6195. doi: https://doi.org/10.1002/2013JD020467

García-Garrido, V. J., Curbelo, J., Mechoso, C. R., Mancho, A. M., & Wiggins, S. (2018). The application of lagrangian descriptors to 3d vector fields. *Regular and Chaotic Dynamics*, *23(5)*, 547-564.

Hadjighasem, A., Karrasch, D., Teramoto, H., & Haller, G. (2016, Jun). Spectral-clustering approach to lagrangian vortex detection. *Phys. Rev. E*, *93*, 063107. doi: 10.1103/PhysRevE.93.063107

Haller, G. (2001). Distinguished material surfaces and coherent structure in three-dimensional fluid flows. *Physica D*, *149*, 248-277.

Haller, G. (2002). Lagrangian coherent structures from approximate velocity data. *Phys. Fluids*, *14*(1851-1861).

Haller, G. (2011). A variational theory of hyperbolic lagrangian coherent structures. *Physica D: Nonlinear Phenomena*, *240*(7), 574-598. doi: https://doi.org/10.1016/j.physd.2010.11.010

Haller, G. (2015). Lagrangian coherent structures. *Annu. Rev. Fluid Mech*, *47*(1), 137–162.

Haller, G., & Beron-Vera, F. J. (2012). Geodesic theory of transport barriers in two-dimensional flows. *Physica D: Nonlinear Phenomena*, *241*(20), 1680-1702. doi: https://doi.org/10.1016/j.physd.2012.06.012

Haller, G., Hadjighasem, A., Farazmand, M., & Huhn, F. (2016). Defining coherent vortices objectively from the vorticity. *Journal of Fluid Mechanics*, *795*, 136–173.

Haller, G., Karrasch, D., & Kogelbauer, F. (2018). Material barriers to diffusive and stochastic transport. *Proceedings of the National Academy of Sciences*, *115*(37), 9074–9079.

Haller, G., & Yuan, G. (2000). Lagrangian coherent structures and mixing in two-dimensional turbulence. *Physica D: Nonlinear Phenomena*, *147*(3), 352-370.

Harriss, R., Browell, E., Sebacher, D., Gregory, G., Hinton, R., Beck, S., ... Shipley, S. (1984). Atmospheric transport of pollutants from North America to the North Atlantic Ocean. *Nature*, *308*(5961), 722–724.

Hersbach, H., Bell, B., Berrisford, P., Horányi, A., Sabater, J. M., Nicolas, J., ... others (2019). Global reanalysis: goodbye ERA-interim, hello ERA5. *ECMWF newsletter*, *159*, 17–24.

Kablick, G. P., Allen, D. R., Fromm, M. D., & Nedoluha, G. E. (2020). Australian Pyrocb Smoke generates synoptic-scale stratospheric anticyclones. *Geophysical Research Letters*, *47*(13), e2020GL088101.

Khaykin, S. M., Godin-Beekmann, S., Hauchecorne, A., Pelon, J., Ravetta, F., & Keckhut, P. (2018). Stratospheric smoke with unprecedentedly high backscatter observed by

lidars above southern france. *Geophysical Research Letters*, *45*(3), 1639-1646.
Khaykin, S. M., Legras, B., Bucci, S., Sellitto, P., Isaksen, L., Tence, F., … others (2020). The 2019/20 Australian wildfires generated a persistent smoke-charged vortex rising up to 35 km altitude. *Communications Earth & Environment*, *1*(1), 1–12.
Lanotte, A. S., Corrado, R., Palatella, L., Pizzigalli, C., Schipa, I., & Santoleri, R. (2016). Effects of vertical shear in modelling horizontal oceanic dispersion. *Ocean Science*, *12*(1), 207–216. Retrieved from `https://os.copernicus.org/articles/12/207/2016/` doi: 10.5194/os-12-207-2016
Lim, E.-P., Hendon, H. H., Boschat, G., Hudson, D., Thompson, D. W., Dowdy, A. J., & Arblaster, J. M. (2019). Australian hot and dry extremes induced by weakenings of the stratospheric polar vortex. *Nature Geoscience*, *12*(11), 896–901.
Lim, E.-P., Hendon, H. H., Butler, A. H., Thompson, D. W. J., Lawrence, Z. D., Scaife, A. A., … Wang, G. (2021). The 2019 southern hemisphere stratospheric polar vortex weakening and its impacts. *Bulletin of the American Meteorological Society*, *102*(6), E1150 - E1171. doi: 10.1175/BAMS-D-20-0112.1
Lopesino, C., Balibrea-Iniesta, F., García-Garrido, V. J., Wiggins, S., & Mancho, A. M. (2017). A theoretical framework for lagrangian descriptors. *International Journal of Bifurcation and Chaos.*, *27(01)*, 1730001.
Mancho, A. M., Wiggins, S., Curbelo, J., & Mendoza, C. (2013). Lagrangian descriptors: A method for revealing phase space structures of general time dependent dynamical systems. *Communications in Nonlinear Science and Numerical Simulations*, *18*(12), 3530-3557.
McWilliams, J. C. (2016). Submesoscale currents in the ocean. *Proceedings of the Royal Society A: Mathematical, Physical and Engineering Sciences*, *472*(2189), 20160117. doi: 10.1098/rspa.2016.0117
Mezić, I., Loire, S., Fonoberov, V. A., & Hogan, P. (2010). A new mixing diagnostic and gulf oil spill movement. *Science*, *330*(6003), 486–489. doi: 10.1126/science.1194607
Peterson, D. A., Campbell, J. R., Hyer, E. J., Fromm, M. D., Kablick, G. P., Cossuth, J. H., & DeLand, M. T. (2018). Wildfire-driven thunderstorms cause a volcano-like stratospheric injection of smoke. *NPJ climate and atmospheric science*, *1*(1), 1–8.
Peterson, D. A., Fromm, M. D., McRae, R. H., Campbell, J. R., Hyer, E. J., Taha, G., … DeLand, M. T. (2021). Australia's Black Summer pyrocumulonimbus super outbreak reveals potential for increasingly extreme stratospheric smoke events. *npj Climate and Atmospheric Science*, *4*(1), 1–16.
Ratna, S. B., Cherchi, A., Osborn, T. J., Joshi, M., & Uppara, U. (2021). The extreme positive Indian Ocean dipole of 2019 and associated Indian Summer Monsoon rainfall response. *Geophysical Research Letters*, *48*(2), e2020GL091497. doi: https://doi.org/10.1029/2020GL091497
Rypina, I. I., & Pratt, L. J. (2017). Trajectory encounter volume as a diagnostic of mixing potential in fluid flows. *Nonlinear Processes in Geophysics*, *24*(2), 189–202. doi: 10.5194/npg-24-189-2017
Rypina, I. I., Scott, S. E., Pratt, L. J., & Brown, M. G. (2011). Investigating the connection between complexity of isolated trajectories and Lagrangian coherent structures. *Nonlinear Processes in Geophysics*, *18*(6), 977–987. doi: 10.5194/npg-18-977-2011
Saji, N., Goswami, B., Vinayachandran, P., & Yamagata, T. (1999). A dipole mode in the tropical indian ocean. *Nature*, *401*(6751), 360–363.
Schlueter-Kuck, K. L., & Dabiri, J. O. (2017). Coherent structure colouring: identification of coherent structures from sparse data using graph theory. *Journal of Fluid Mechanics*, *811*, 468–486. doi: 10.1017/jfm.2016.755
Schwartz, M., Livesey, N., & Read, W. (2020). *MLS/Aura Level 2 Geopotential Height V005, Greenbelt, MD, USA, Goddard Earth Sciences Data and Information Services Center (GES DISC).* `10.5067/Aura/MLS/DATA2507`. ([Accessed: 8-April-2022])
Serra, M., & Haller, G. (2016). Objective eulerian coherent structures. *Chaos: An Interdisciplinary Journal of Nonlinear Science*, *26*(5), 053110. doi: 10.1063/1.4951720
Shadden, S. C., Lekien, F., & Marsden, J. E. (2005). Definition and properties of Lagrangian

Coherent Structures from finite-time Lyapunov exponents in two-dimensional aperiodic flows. *Physica D*, *212*, 271-304.

Solomon, S., Dube, K., Stone, K., Yu, P., Kinnison, D., Toon, O. B., ... Degenstein, D. (2022). On the stratospheric chemistry of midlatitude wildfire smoke. *Proceedings of the National Academy of Sciences*, *119*(10), e2117325119. Retrieved from `https://www.pnas.org/doi/abs/10.1073/pnas.2117325119` doi: 10.1073/pnas.2117325119

Stocker, M., Ladstädter, F., & Steiner, A. K. (2021). Observing the climate impact of large wildfires on stratospheric temperature. *Scientific reports*, *11*(1), 1–11.

Sulman, M. H., Huntley, H. S., Lipphardt, B., & Kirwan, A. (2013). Leaving flatland: Diagnostics for lagrangian coherent structures in three-dimensional flows. *Physica D: Nonlinear Phenomena*, *258*, 77-92. doi: https://doi.org/10.1016/j.physd.2013.05.005

van der Velde, I. R., van der Werf, G. R., Houweling, S., Maasakkers, J. D., Borsdorff, T., Landgraf, J., ... others (2021). Vast CO2 release from Australian fires in 2019–2020 constrained by satellite. *Nature*, *597*(7876), 366–369.

VIIRS. (2022). *NRT VIIRS 375 m active fire product VJ114IMGTDL_NRT distributed from NASA FIRMS.* `https://earthdata.nasa.gov/firms`. ([Online; accessed 25-May-2022]) doi: 10.5067/FIRMS/VIIRS/VJ114IMGT_NRT.002

von Schoenberg, P., Tunved, P., Grahn, H., Wiedensohler, A., Krejci, R., & Brännström, N. (2021). Aerosol dynamics and dispersion of radioactive particles. *Atmospheric Chemistry and Physics*, *21*(6), 5173–5193. doi: 10.5194/acp-21-5173-2021

Wang, G., & Cai, W. (2020). Two-year consecutive concurrences of positive Indian Ocean Dipole and central pacific el Niño preconditioned the 2019/2020 Australian "black summer" bushfires. *Geoscience Letters*, *7*(1), 1–9.

Yang, Y., Xie, S.-P., Wu, L., Kosaka, Y., Lau, N.-C., & Vecchi, G. A. (2015). Seasonality and predictability of the indian ocean dipole mode: ENSO forcing and internal variability. *Journal of Climate*, *28*(20), 8021–8036.

Yu, P., Davis, S. M., Toon, O. B., Portmann, R. W., Bardeen, C. G., Barnes, J. E., ... Rosenlof, K. H. (2021). Persistent stratospheric warming due to 2019–2020 australian wildfire smoke. *Geophysical Research Letters*, *48*(7), e2021GL092609. doi: https://doi.org/10.1029/2021GL092609

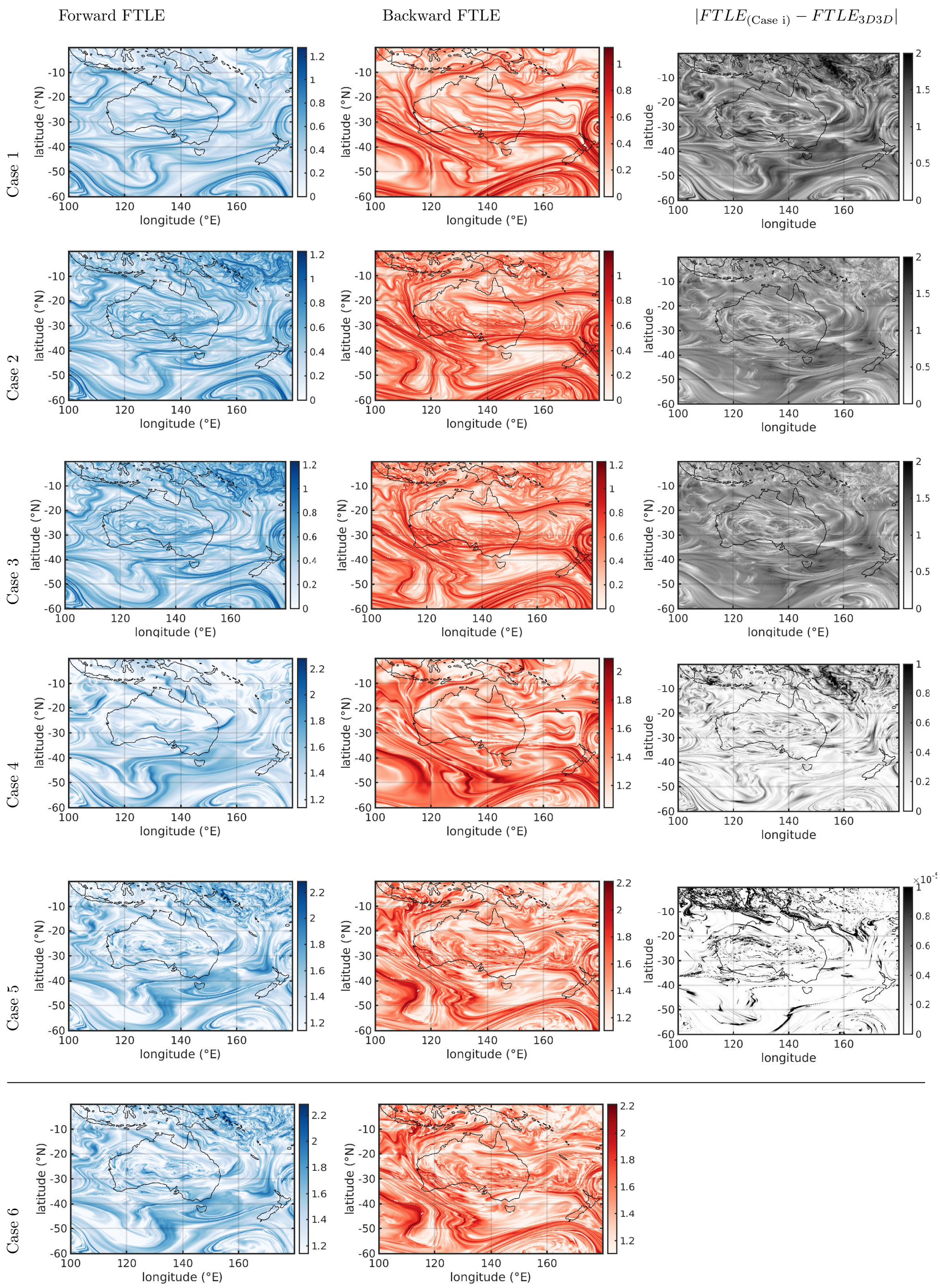

Figure 1. Forward (first column) and backward (second column) FTLE computed with τ=5 days for the different formulations at 5km above the sea-level. Each row corresponds to one of the FTLE formulations described in the text. To quantify the effects of vertical shear and vertical velocity the third column represents the absolute error between the forward FTLE for the corresponding case to the fully 3D FTLE (case 6).

(a) 22 December 2019

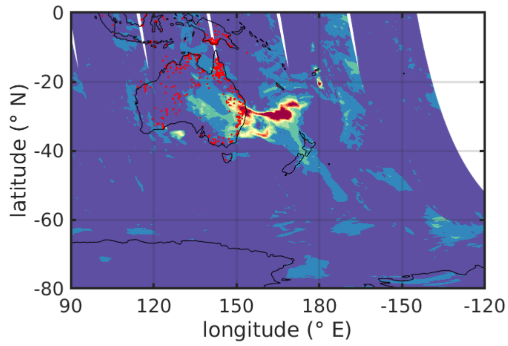

(b) 31 December 2019

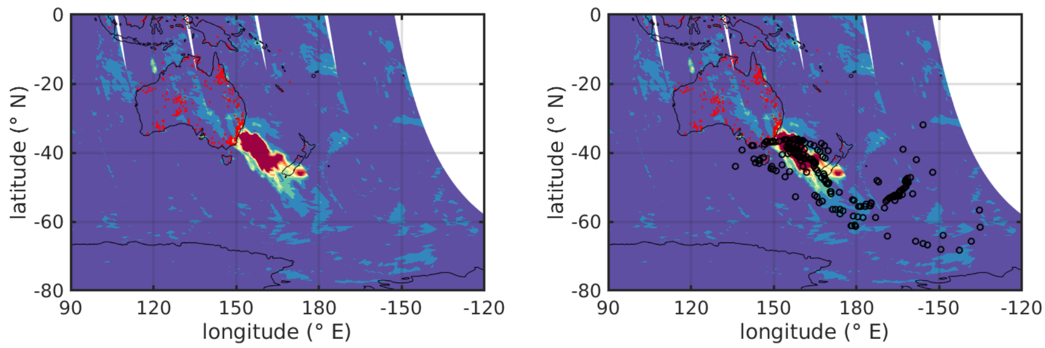

Figure 2. OMPS Aerosol index colormap over Australia during the days (a) 22 December 2019 and (b) 31 December 2019. The red dots are fires/hotspots from VIIRS given by thermal anomalies. Maroon color marks the smoke plume. The black dots are the positions on the corresponding day of the backtracked pollutant parcel trajectories starting on January 6 discussed in section 4.2.

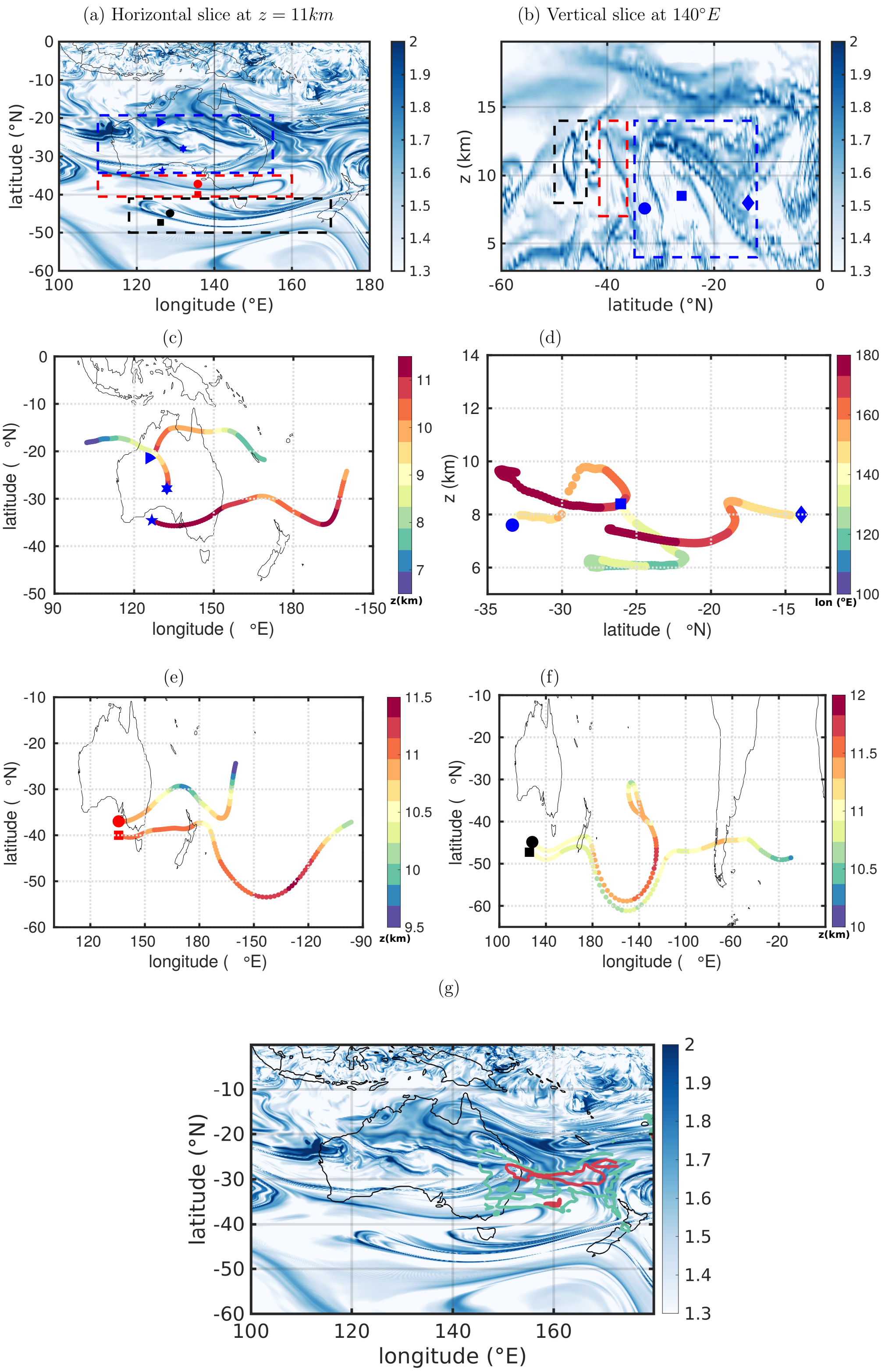

Figure 3. Horizontal (a) and vertical (b) slices of the 3D forward FTLE computed the day December 22, 2019 with $\tau = 5$ days at $z = 11km$ height and a fix longitude 140° E, respectively. The boxes highlight the three coherent structures described in the text. The dots correspond to the initial position of forward parcels trajectories that are shown in panels (c-f) as examples of dynamics in the different regions. Panel (g) shows where the main Aerosol plume (figure 2a) is located with respect to the LCSs on December 22.

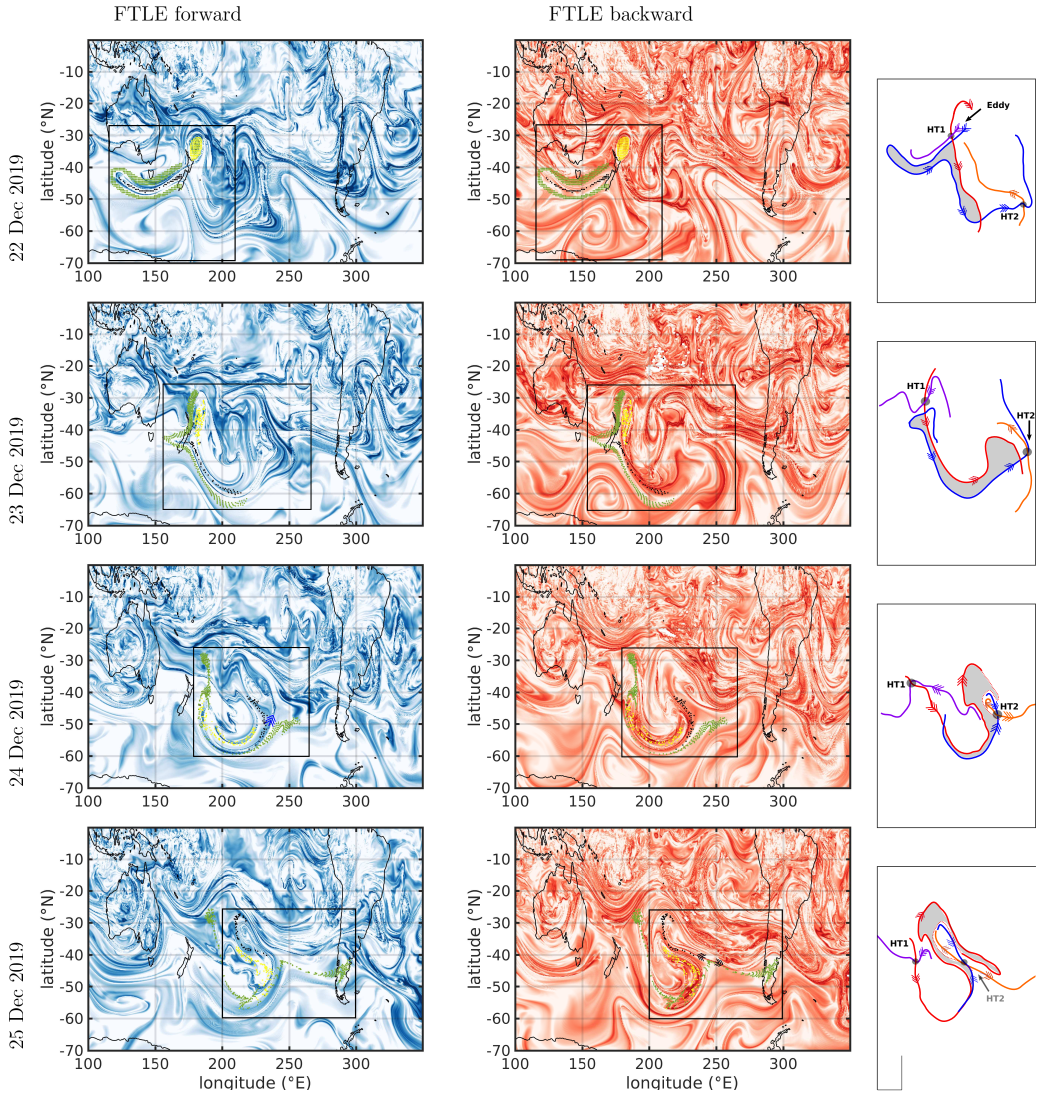

Figure 4. Snapshot of the time evolution of FTLE forward (first column) and backward (second column). Panel displays forward parcel trajectories at 11km that are initialized on December 22, 2018. Green color identifies parcels that on December 22 are outside the tubular structure formed by the stable manifold but close to it. Yellow color identifies parcels on the eddy structure and black color identifies parcels inside the tube. The third column shows a diagram of the relative position of the stable (in purple and blue) and unstable (in red and orange) manifolds associated with the hyperbolic trajectory HT1 and HT2, respectively.

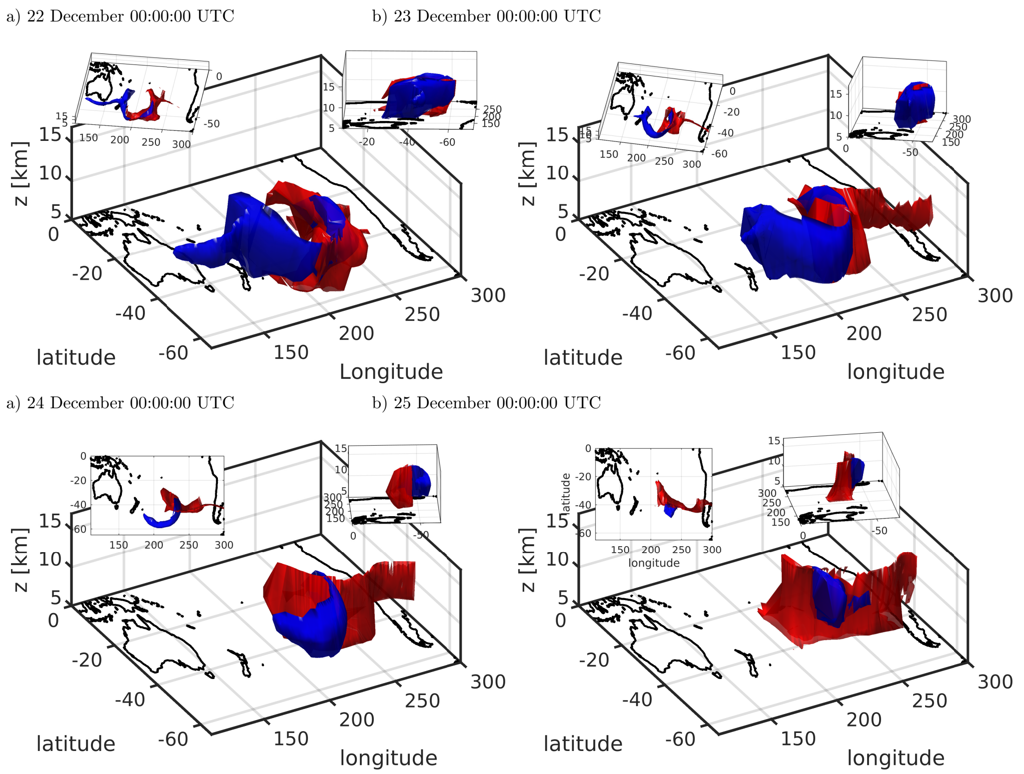

Figure 5. Time evolution of the stable (blue) and (unstable) manifold in 3D obtained by the algorithm described in section 4.1.

Figure 6. a) Plume tracking map of aerosol data with MLS pro l $H_2O > 7$ ppmv and CO > 50 ppbv and geopotential height between 15km and 35km. Path 1 (green) and Path 2 (blue) are described in the text. b) Forward trajectories starting January 6, 2020 (magenta dots) computed by adding a constant buoyancy of 0:0022m=s. c) Forward trajectories starting January 6, 2020 computed with 3D velocity without buoyancy. d) Backward trajectories also starting January 6, 2020 (magenta dots) computed by adding a constant buoyancy of 0:0052m=s. Backward and forward paths are in red and blue respectively. The color of the points indicates the height in km (color bar) and the color of its line the corresponding day: 31 (yellow) of December, 6 (magenta) and 27 (black) of January, 17 (blue) and 26 February (cyan).

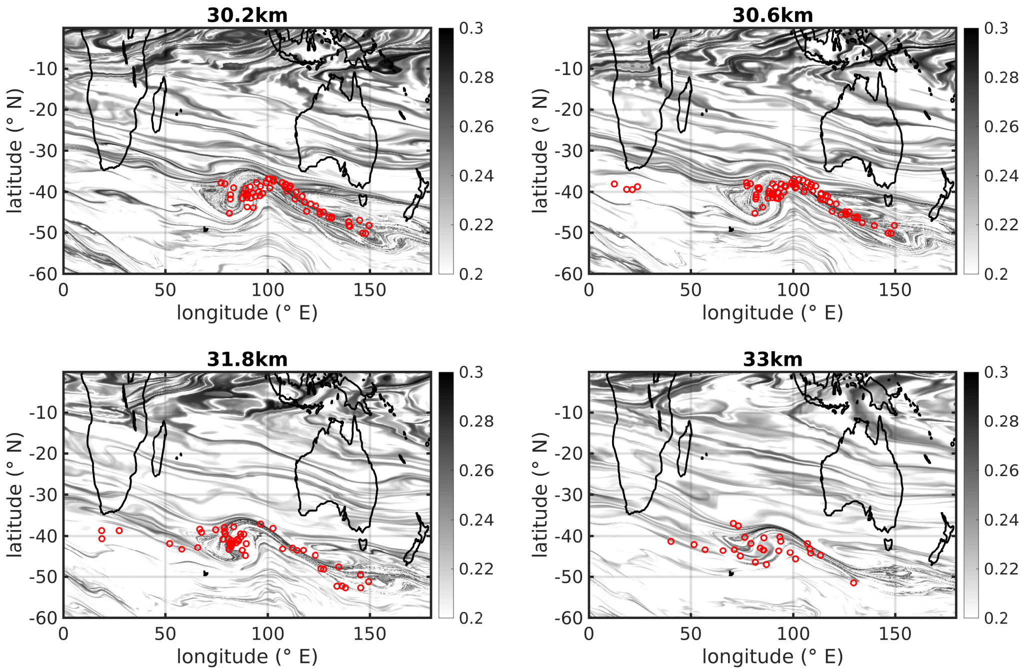

Figure 8. Longitude-latitude section of Backward FTLE (color background) computed in 3D with buoyancy with $\tau = 40$ days on 26 of February 2020. The red dots are the final position of the trajectory that started on January 6 represented in the figure 6(b).